33RD CONGRESS
OF THE INTERNATIONAL COUNCIL
OF THE AERONAUTICAL SCIENCES
STOCKHOLM, SWEDEN, 4-9 SEPTEMBER, 2022

ICAS 2022 SWEDEN

DIRECT NUMERICAL SIMULATIONS OF A THICK, ROTATING AIRFOIL AT A LOW REYNOLDS NUMBER

Thales Coelho Leite Fava, Dan Henningson & Ardeshir Hanifi

FLOW, Department of Engineering Mechanics, KTH Royal Institute of Technology, Stockholm, Sweden

Abstract

Direct numerical simulations of the flow around an FFA-W3 series airfoil at a chord Reynolds number of $100,000$ are performed to study the effects of rotation on flow over a section of a rotating wing. In order to achieve this goal, three simulations with different rotation speeds (and corresponding angles of attack) are carried out. Three additional simulations with the same angles of attack of the former but without including Coriolis and centrifugal forces are also computed. It is shown that rotation moves the transition location upstream on the suction side for low angles of attack, and on the pressure side, due to the enhancement of the shear-layer instability and its spanwise modulation. Nevertheless, rotation delays transition on the suction side for larger angles of attack. The reason for this change is most likely the fact that the shear-layer instability is much stronger in this case, and it is not bypassed by instabilities generated by rotation such as that from the inflectional spanwise velocity profiles. However, the latter can reduce the shear in the separation bubble, mitigating the rapid growth of the former. The onset of separation is not changed by rotation, but the trailing edge of the separation bubble is displaced downstream because of an enhanced reverse flow. The lift is only significantly affected by rotation when there are large separation regions on both suction and pressure surfaces, promoting its reduction.

Keywords: Direct numerical simulations, flow instability, rotating wings, separation bubble instability

1. Introduction

Airfoils under rotation experience distinct aerodynamic behavior compared to non-rotating profiles, which was first noticed as an increase in the lift of aircraft propellers [1]. Theoretical studies showed that rotation promotes separation delay or even suppression if the adverse pressure gradient is sufficiently small [2] and that the cross-flow velocity component generated by rotation plays a pivotal role in this phenomenon [3]. Experiments demonstrated that the separation point is moved further downstream when the rotation is increased [4]. Moreover, the lift increase was shown to be related to the magnitude of the spanwise component [5]. The growth in lift and delay of the stall were also attributed to the reduction in the pressure on the suction side and the acceleration of the boundary layer in the streamwise direction by the Coriolis force [6]. Despite promoting the movement of fluid from separated areas in the spanwise direction, a phenomenon known as centrifugal pumping, experiments indicated that the centrifugal effects are relatively unimportant regarding the change in the aerodynamic forces over the blade [7]. Experimental [8, 9] and numerical [10] studies showed that, in the separation region of a rotating blade, there is the formation of counter-rotating vortices, which are periodic in the spanwise direction and roughly aligned with the streamwise one. Additionally, the rise in the Reynolds number [4, 11] and turbulence intensity [12] seems to reduce the effects of rotation on the flow.

The considerable increase in the computational power in the last decades has allowed more detailed numerical investigations of these effects. Many studies in this domain were performed for wind-turbine blades since flow separation, which often occurs in the normal range of operation of these wings, enhances the rotation effects. In contrast, attached boundary layers are little affected by them

[13, 7]. Those numerical studies can be classified in increasing order of complexity, ranging from quasi-3D models of the Reynolds averaged Navier-Stokes (RANS) equations [14, 15], full 3D RANS simulations of parts of the blade or the entire rotor [16, 17, 18, 19, 20], and a blend between RANS and large-eddy simulations (LES) such as the detached eddy simulation (DES) approach [21, 22, 23]. These studies were able to identify a significant cross-flow velocity component in the separation flow region and rotational augmentation. Nevertheless, deeper insight into the mechanisms behind these phenomena was only gained with direct numerical simulations (DNS) such as those performed for wind turbine blades [24, 25], and marine propellers [26]. In particular, some of these works showed that the separation delay was caused by an early transition to turbulence triggered by a cross-flow instability [27] due to the cross-flow velocity component generated by rotation [24, 26]. Furthermore, stability analyses, accounting for rotation effects, of velocity profiles from solving the boundary layer equations showed that highly-oblique modes, i.e., modes with wavevectors significantly misaligned with the streamwise direction, triggered transition in the inboard part of the blade [28]. The modes for a non-rotating flow were shown to be much less oblique.
Nonetheless, the works performed so far using DNS to study the effects of rotation on airfoil performance did not investigate the role of the change in the rotation speed and angle of attack on the flow physics and airfoil performance. This point is relevant because a propeller or wind turbine blade does not operate at a single rotation speed and may undergo different angles of attack at each rotation condition. For this reason, the current work attempts to shed light on this problem with a particular focus on the characterization of the flow field for each of these cases. In order to reach this goal, a thick wind-turbine airfoil, prone to separation, is studied through DNS at three different angles of attack and rotation speeds. In addition, three non-rotating control cases are also analyzed, with the same angles of attack as the rotating cases. The Reynolds number of $100,000$ is relatively low due to the high computational cost involved in simulations at higher values of this parameter.

2. Numerical Setup

The selected airfoil was a blend of 96% of FFA-W3-241, and 4% of the FFA-W3-301 airfoils [29], corresponding to the airfoil at 68% of the radius of the DTU 10-MW Reference Wind Turbine [30]. The chord Reynolds number was $100,000$. The simulations were carried out in the rotating frame of reference using the incompressible spectral-element Navier-Stokes solver Nek5000 [31]. Figure 1 shows this frame of reference. The picture on the left-hand side describes the cut of the blade by a cylindrical shell with a centerline aligned with the rotation axis. This is referred to as the physical frame of reference. AoA is the angle of attack, ϕ is the twist angle, ω is the rotation vector, U_∞ is the relative inflow velocity, and L and D are the lift and drag forces. The picture on the right-hand side describes the frame of reference used in the simulation, which is rotated with an angle $\phi = 4.8^\circ$ in relation to the physical frame of reference, such that the horizontal direction x is aligned with the chord. Notice that the positive z direction points in the direction out of the page, which corresponds to the decreasing radii direction. The radial position of the blade is $r = 0.68R$, where R is the radius of the blade, with r assumed to be constant inside the simulated domain. The width of the domain (in the z direction) is 0.1. If not explicitly specified, the variables are non-dimensionalized with the airfoil chord and free-stream velocity. The Coriolis and centrifugal forces were added as volume sources in the momentum equations that are given by

$$\begin{aligned} f_x &= -2\omega_x u_z, \\ f_y &= +2\omega_y u_z, \\ f_z &= -r\omega^2 + 2\omega_y u_x - 2\omega_x u_y. \end{aligned} \tag{1}$$

The initial and boundary conditions were obtained from RANS simulations computed with the solver Fluent [32]. This allowed using a smaller domain of only 0.6 chord on each side. The outlet was located 1.5 chords downstream of the trailing edge. The mesh consisted of 246,000 spectral elements with polynomial degree 7, which amounted to approximately 126 million grid points. Since the spectral element method employed in the simulations is almost devoid of noise, transition might not have been

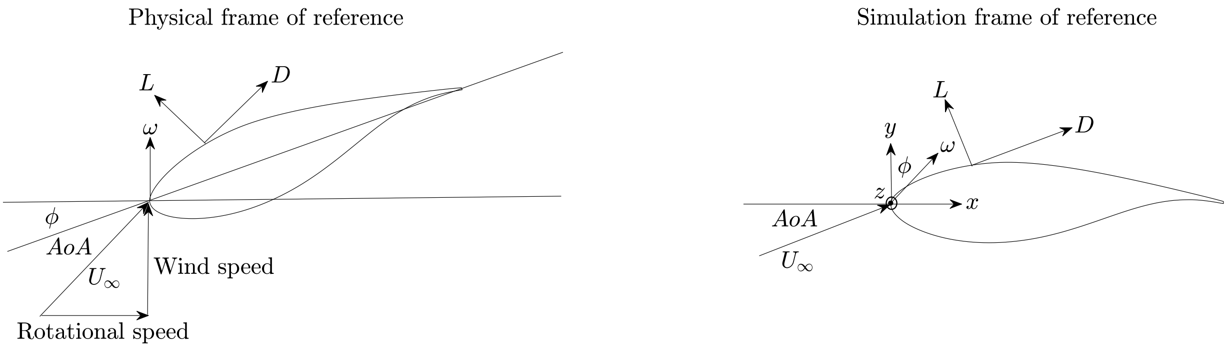

Figure 1 – Physical and simulation frames of references.

triggered. For this reason, 32 Fourier modes evenly spaced in frequency with amplitude 1×10^{-6} were introduced close to the surface at around 5% of the chord on the suction side.
Table 1 summarizes the studied cases. λ is the tip-speed ratio, defined as $(\omega\, R)/u_{wind}$, where ω is the rotation speed, R is the radius of the blade, and u_{wind} is the wind speed. $u_{rotation} = \omega\, r$ is the rotation velocity, where $r = 0.68\, R$. u_{x_∞} and u_{y_∞} are the relative, undisturbed inflow velocities in the x and y directions. ω_x and ω_y are the rotation speeds in the x and y directions.

AoA (°)	λ	u_{wind}	$u_{rotation}$	u_{x_∞}	u_{y_∞}	ω_x	ω_y
12.8	4.6	0.30	0.95	0.9751	0.2219	0.0044	0.0521
12.8	0.0	0.30	0.95	0.9751	0.2219	0	0
4.2	9.3	0.16	0.98	0.9973	0.0737	0.0045	0.0540
4.2	0.0	0.16	0.98	0.9973	0.0737	0	0
1.2	13.9	0.11	0.99	0.9998	0.0217	0.0046	0.0544
1.2	0.0	0.11	0.99	0.9998	0.0217	0	0

Table 1 – Parameters of the studied cases.

3. Results

3.1 Mean-flow characteristics

The distributions of pressure coefficient (C_p) are shown in Fig. 2. The $AoA = 12.8°$ case displays an APG acting on the entirety of the suction side (lower part of the curves), with a sharp rise in pressure in the region $x = 0.40-0.46$ and $x = 0.36-0.42$ for the rotating and non-rotating cases, respectively. These locations are inside the LSB, and the pressure rise is due to the low-momentum flow inside the recirculation zone. The fact that the rise in pressure occurs more downstream for $\lambda \neq 0$ is related to the downstream displacement of the LSB in this case. In the region upstream of the LSB, the rotating case presents a higher pressure on the suction side, which can be caused by the retardation of the flow due to the Coriolis force in the x direction. The differences between the pressure coefficient for rotating and non-rotating cases are insignificant downstream of the LSB, where the flow is turbulent.
On the pressure side (upper part of the curves), one can observe an APG up to the stagnation point, which generates a leading-edge separation bubble, followed by a region of favorable pressure gradient (FPG) extending up to $x = 0.37$ for $\lambda \neq 0$ and $x = 0.38$ for $\lambda = 0$. Downstream of this point, a mild APG acts on the flow. Close agreement between rotating and non-rotating pressure coefficient distributions is noticed.
Considering the suction side of the $AoA = 4.2°$ case, it is possible to notice that there is a region of FPG up to $x = 0.21$ for $\lambda \neq 0$ and $x = 0.20$ for $\lambda = 0$, where a mild APG starts to act. Moreover, the rotating case indicates higher pressure than the non-rotating one, which can be attributed to the flow retardation due to rotation, as discussed for the $AoA = 12.8°$ case. Moreover, separation cannot be identified from the pressure coefficient, and the curves for both $\lambda \neq 0$ and $\lambda = 0$ cases collapse in the turbulent region. On the pressure side, an FPG is present until $x = 0.26$ for $\lambda \neq 0$ and $x = 0.27$

for $\lambda = 0$, followed by a mild APG downstream. The C_p for the rotating case is lower than that of the non-rotating case. Nonetheless, this difference is small, apart from $x > 0.7$, where there is a strong separation region and the flow tends to be accelerated in the x direction by the rotation. The $AoA = 1.2°$ case presents a suction side with an FPG up to $x = 0.27$, followed by a low APG until the LSB reattachment at $x = 0.78 - 0.79$, where there pressure gradient becomes more adverse. On the pressure side, the FPG region goes up to $x = 0.22$, followed by a low APG. The rotating and non-rotating C_p curves are in close agreement for both sides of the airfoil. For all cases, the velocity profiles become inflectional and, therefore, possibly unstable according to Rayleigh's criterion, 1% of the chord downstream of the location where the APG starts.
Therefore, the pressure coefficient is affected by rotation by means of the displacement of the LSB and by the acceleration/retardation of the flow by the Coriolis force that induces a drop/rise in C_p inside/outside the reverse flow region compared to the non-rotating case.

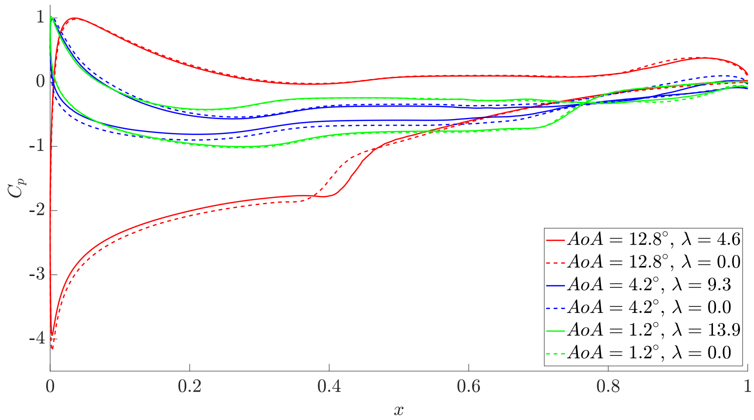

Figure 2 – Pressure coefficient.

The friction coefficient (C_f) distributions on the suction and pressure sides are presented in Fig. 3. Considering the suction side of the $AoA = 12.8°$ case, one can notice that the C_f is higher for the rotating case upstream of $x = 0.23$, indicating a higher acceleration of the flow. Mild flow separation occurs at $x = 0.23$, marked by the negative C_f, for rotating and non-rotating cases. However, these cases experience strong separation at $x = 0.38$ and $x = 0.34$, respectively, where it is possible to notice a sharp drop in the C_f. Although taking place more downstream, separation for the rotating case is more intense, i.e., it presents a stronger reverse flow. Transition occurs in this region of strong negative C_f and leads the flow to reattach at $x = 0.46$ and $x = 0.42$ for $\lambda \neq 0$ and $\lambda = 0$, which is followed by a large increase in the friction coefficient that is characteristic of turbulent flow.
The results for the suction side of the $AoA = 4.2°$ case indicate separation at $x = 0.34$, and the formation of three reverse flow cells located at $x = 0.34 - 0.63$, $x = 0.63 - 0.81$, and $x = 0.81 - 0.98$. The last cell is the one that presents the highest reverse flow, but transition occurs within the first one. The friction coefficient distributions for the rotating and non-rotating cases are very close to each other up to the end of the first cell; further downstream, the reverse flow is stronger in the non-rotating case, leading to an overall more negative C_f. Regarding the $AoA = 1.2°$ case, separation occurs at $x = 0.38$, and three reverse flow cells can also be identified at $x = 0.38 - 0.56$, $x = 0.56 - 0.66$, and $x = 0.66 - 0.78$. Transition takes place in the first two cells and reattachment at the end of the third cell. The $\lambda \neq 0$ and $\lambda = 0$ cases display close C_f distributions.
Analyzing the pressure side of the $AoA = 12.8°$ case, one can notice a leading-edge separation bubble up to 4% of the chord. The flow separates again at $x = 0.47$ for $\lambda \neq 0$ and $x = 0.48$ for $\lambda = 0$, with a higher reverse flow region occurring between $x = 0.74$ and $x = 0.92 - 0.90$. The C_f for the rotating and non-rotating cases are close to each other for regions upstream of separation or with small separation, such as $x < 0.68$. Considering the $AoA = 4.2°$ case, separation occurs at $x = 0.36$ for $\lambda \neq 0$ and at $x = 0.37$ for $\lambda = 0$, but strong reverse flow only occurs in the region from $x = 0.58$ to $x = 0.94 - 0.97$. The differences between $\lambda \neq 0$ and $\lambda = 0$ results are only significant for $x > 0.58$, where the rotating case presents more negative C_f (stronger reverse flow). The results for $AoA = 1.2°$

indicates separation starting at $x = 0.32$. However, in the region $x = 0.49 - 0.63$, there are several local reattachment zones that are more pronounced in the rotating case. The stronger reverse flow zone inside the LSB occurs for $x > 0.70$, where the C_f for the non-rotating case becomes more negative (more substantial reverse flow).

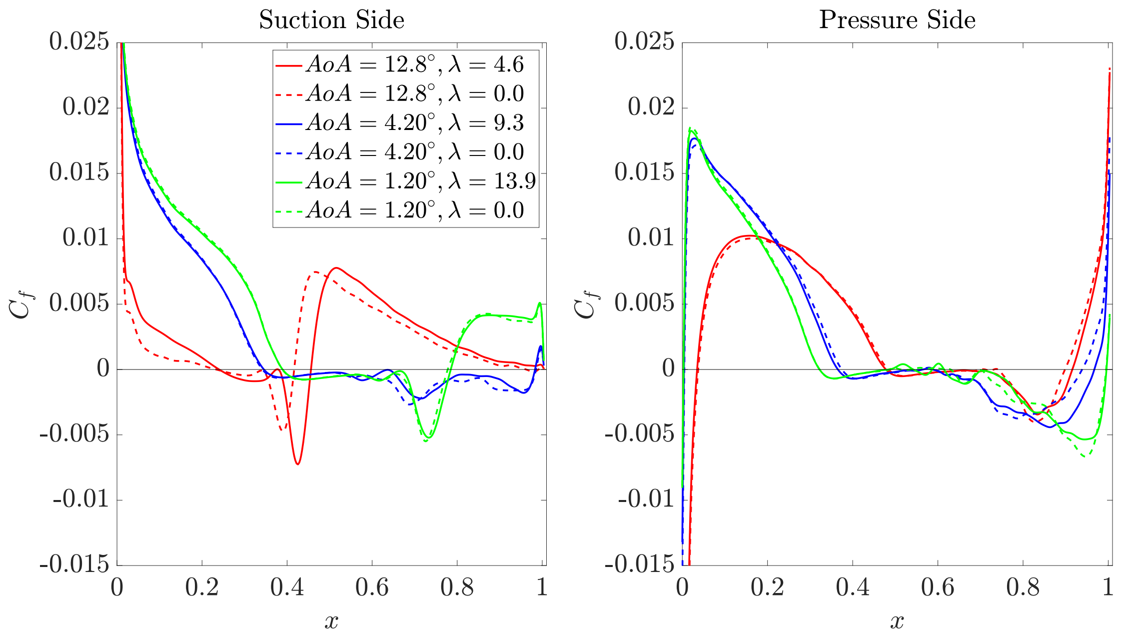

Figure 3 – Friction coefficient.

Tables 2 and 3 summarizes some characteristics of the LSB and transition on the suction and pressure sides, respectively. x_{b_1} and x_{b_2} are the leading and trailing edges of the separation region. $x_{y_{max}}$ and y_{max} are the streamwise location of the separation region maximum height and the value of this height. x_a and x_i are the positions downstream of which there is an APG acting on the flow and the velocity profiles are inflectional. x_{tr_1} is the transition location computed as the x location where $-\overline{uv}/U_\infty^2 = 0.001$ [33]. This method is adequate for identifying the beginning of transition as it tends to be sensitive to the growth of perturbations. x_{tr_2}, is defined as the x station of the maximum boundary-layer aspect ratio $H = \delta^*/\theta$ [34], with δ^* being the displacement thickness and θ being the momentum thickness. This methodology is better for identifying the later stages of transition, where the shape of the mean velocity profiles has significantly changed to turbulent.

Table 2 – Characteristics of the LSB and transition on the suction side.

AoA (°)	λ	x_{b_1}	x_{b_2}	$x_{y_{max}}$	$y_{max} \times 10^2$	y_{max}/δ^*	x_a	x_i	x_{tr_1}	x_{tr_2}
12.8	4.6	0.23	0.46	0.40	0.75	0.70	0.00	0.00	0.35	0.39
12.8	0.0	0.23	0.42	0.36	0.43	0.54	0.00	0.00	0.33	0.36
4.2	9.3	0.34	-	0.70	2.65	0.51	0.21	0.22	0.35	0.50
4.2	0.0	0.34	-	0.68	2.72	0.56	0.20	0.21	0.36	0.50
1.2	13.9	0.38	0.79	0.70	1.78	0.71	0.27	0.28	0.40	0.59
1.2	0.0	0.38	0.78	0.70	1.75	0.71	0.27	0.28	0.41	0.59

The lift (C_L) and drag (C_D) coefficients as a function of the angle of attack, as well as the percentual difference between the non-rotating and rotating C_L (ΔC_L) and C_D (ΔC_D) are displayed in Table 4. For the $AoA = 12.8°$ case, the rotating case presents a C_L 2.14% lower than the non-rotating one. The reason for this phenomenon was previously discussed, and it is linked to the retardation of the flow on the suction side due to the Coriolis force, which leads to an increase in the local C_p, and the acceleration of the flow on the pressure side that promotes a reduction in this parameter. The drag

Table 3 – Characteristics of the LSB and transition on the pressure side.

AoA (°)	λ	x_{b_1}	x_{b_2}	$x_{y_{max}}$	$y_{max} \times 10^2$	y_{max}/δ^*	x_a	x_i	x_{tr_1}	x_{tr_2}
12.8	4.6	0.47	0.92	0.78	3.75	0.89	0.37	0.38	0.56	0.70
12.8	0.0	0.48	0.90	0.78	3.60	0.90	0.38	0.39	0.61	0.71
4.2	9.3	0.36	0.97	0.79	6.79	0.87	0.26	0.27	0.37	0.71
4.2	0.0	0.37	0.94	0.75	5.89	0.87	0.27	0.27	0.40	0.71
1.2	13.9	0.32	-	0.83	10.66	0.93	0.22	0.23	0.35	0.75
1.2	0.0	0.32	-	0.83	10.71	0.94	0.22	0.23	0.35	0.72

coefficient is 18.43% higher in the non-rotating case. Considering the $AoA = 4.2°$ case, the C_L drops for the rotating and non-rotating simulations compared to the $AoA = 12.8°$ case due to massive flow separation on the suction side (without reattachment) and pressure side. Nevertheless, the drop in the C_L is larger for the rotating case, which presents a lift 54.55% lower than the non-rotating one. This phenomenon is caused by the same mechanism as that for the $AoA = 12.8°$ case, but the effect is exacerbated in the $AoA = 4.2°$ case by the occurrence of a large area of flow separation. The rotating simulation presents a drag 0.58% lower than the non-rotating one. Considering the $AoA = 1.2°$ case, the lift coefficient for $\lambda \neq 0$ and $\lambda = 0$ is practically the same, which is expected given the collapse of the C_p for the rotating and non-rotating simulations. This highlights the dependence of the rotation effects on the strength of the separation region. The C_D for the rotating case is 1.61% lower than the non-rotating one.

Table 4 – Lift (C_L) and drag (C_D) coefficients, and percentage difference between rotating and non-rotating cases (ΔC_L and ΔC_D).

AoA (°)	λ	C_L	ΔC_L	$C_D \times 10^2$	ΔC_D
12.8	4.6	1.40	-2.14%	6.51	18.43%
12.8	0.0	1.43		5.31	
4.2	9.3	0.22	-54.55%	8.66	-0.58%
4.2	0.0	0.34		8.71	
1.2	13.9	0.38	0.00%	6.83	-1.61%
1.2	0.0	0.38		6.94	

3.2 Detailed flow characteristics

Figure 4 portrays flow snapshots of isosurfaces of streamwise velocity perturbations colored by the mean streamwise velocity at an arbitrary time. The left column shows the non-rotating cases, and the right one results of simulations with rotation. Each row corresponds to an angle of attack. Considering the $AoA = 12.8°$ case, transition occurs abruptly on the suction side at around 40% of the chord for both non-rotating and rotating cases. The rapid destabilization of the flow may result from a strong reverse flow in a separation bubble, enabling an inviscid instability mechanism. The transitioning flow rapidly reattaches due to the high-momentum fluid entrained by the vortices at the trailing edge of the laminar separation bubble (LSB) [34]. However, the LSB is larger in the rotating case, which is highlighted by the more pronounced negative-velocity region displayed by the near-wall contours. Visualizations of several snapshots of streamwise velocity perturbations indicate a path of high-momentum fluid being entrained into the separation bubble in the non-rotating case, which is not noticed in the rotating one. The reason for this difference will be analyzed later. The pressure side for the $AoA = 12.8°$ case is characterized by flow separation observed around 70% of the chord for both $\lambda \neq 0$ and $\lambda = 0$ cases, which seems to lead to transition. The flow reattaches close to the trailing edge.

The $AoA = 4.2°$ case indicates flow separation on the suction side around 50% of the chord for both rotating and non-rotating cases, which is noticed in the figure as a thread of high-magnitude perturbations detached from the surface. Further downstream, one can see the breakdown to turbulence at around 60% of the chord, which is further downstream than in the $AoA = 12.8^\circ$ case, induced by the shear-layer instability. The later transition in the current case may be due to a less intense adverse pressure gradient (APG) compared to the higher AoA simulation. In addition, the flow does not reattach as seen by the negative values of velocity as downstream as the airfoil trailing edge. It is also possible to observe the shedding of vortices appearing as rings in the isosurfaces, particularly in the rotating case. These vortices are characteristic of instability of the Kelvin-Helmholtz (KH) type that develops on the shear layer leading to its roll-up. Regarding the pressure side of the $AoA = 4.2^\circ$ case, there is flow separation at approximately mid-chord for both $\lambda \neq 0$ and $\lambda = 0$ cases, and a large region of reverse flow is formed until the airfoil trailing edge, where the flow seems to reattach. The shear-layer roll-up can also be noticed on the pressure side, where large vortices are formed at the edge of the detached shear layer and advected downstream.

The $AoA = 1.2^\circ$ case displays separation at approximately mid-chord on the suction side, visible as a thread of high-amplitude perturbations released from the surface. However, the separation region is smaller in the streamwise and normal directions. The flow reattaches around 80% of the chord, and the shedding of turbulent vortices is more pronounced downstream of this point. The flow is characterized by massive separation starting around mid-chord on the pressure side, which persists downstream of this point and does not reattach. Large spanwise vortices are formed on the detached shear layer, but this phenomenon is less pronounced than in the $AoA = 4.2^\circ$ case. Moreover, the rotating case seems to display a more extensive region with reverse flow.

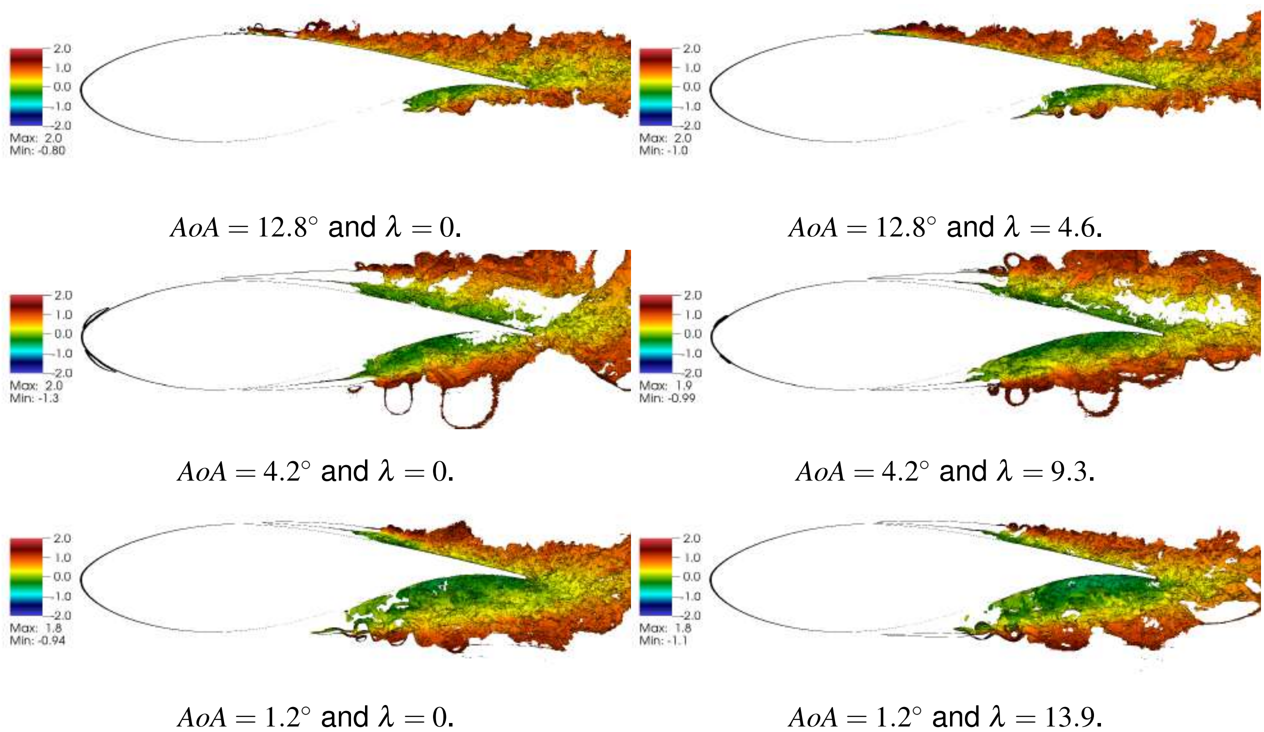

$AoA = 12.8^\circ$ and $\lambda = 0$. $AoA = 12.8^\circ$ and $\lambda = 4.6$.

$AoA = 4.2^\circ$ and $\lambda = 0$. $AoA = 4.2^\circ$ and $\lambda = 9.3$.

$AoA = 1.2^\circ$ and $\lambda = 0$. $AoA = 1.2^\circ$ and $\lambda = 13.9$.

Figure 4 – Instantaneous isosurfaces of streamwise velocity perturbations ($u = U - \langle U \rangle_{z,t}$) colored by the mean streamwise velocity ($\langle U \rangle_{z,t}$).

In order to obtain a more precise picture of the flow and highlight the differences between the non-rotating and rotating cases, the spanwise and time-averaged streamwise velocity contours on the suction and pressure sides are presented in Figs. 5 and 6, respectively. The displacement thickness is represented with a black line, and the separation bubble edge is depicted with a red line (curve over which $\int_0^\delta U dy = 0$). Considering the suction side of the $AoA = 12.8^\circ$ case, one can notice that the LSB starts at $x = 0.23$ in both $\lambda \neq 0$ and $\lambda = 0$ simulations as a response to an APG acting throughout the whole extent of the airfoil; however, the separation region extends more downstream in the rotating case, with a trailing edge at $x = 0.46$ compared to $x = 0.42$ in the non-rotating one. Furthermore, the LSB presents a larger maximum height for $\lambda \neq 0$ ($y_{max}/\delta^* = 0.70$ at $x_{y_{max}} = 0.40$) than for $\lambda = 0$ ($y_{max}/\delta^* = 0.54$ at $x_{y_{max}} = 0.36$), where δ^* is the displacement thickness. One can also notice from Fig. 5 that δ^* increases substantially downstream of $x_{y_{max}}$, indicating transition to turbulence around this location. Nevertheless, flow instability possibly starts much upstream because the velocity profiles are inflectional downstream of the airfoil leading edge.

Considering the suction side in the $AoA = 4.2°$ case, one can notice that separation starts at $x = 0.34$, and the flow does not reattach both for $\lambda \neq 0$ and $\lambda = 0$. Separation is engendered by an APG acting downstream of $x = 0.21$ and $x = 0.20$ for those two cases. In addition, the region with reverse flow is relatively large compared to the $AoA = 12.8°$ case. The separation bubble consists of three cells, identified in the contours as stronger reverse flow regions and lumps in the red line that are more visible in the rotating case. This may be caused by a feedback mechanism between separation and transition, in which the unstable, separated shear-layer leads to an increased momentum mixing and local reduction in the LSB (i.e., lower reverse flow), whose base-flow is less unstable, which in turn mitigates the shear-layer instability. The maximum height of the LSB is $y_{max}/\delta^* = 0.51$ at $x_{y_{max}} = 0.70$ and $y_{max}/\delta^* = 0.56$ at $x_{y_{max}} = 0.68$ for $\lambda \neq 0$ and $\lambda = 0$, respectively.

The suction side of the $AoA = 1.2°$ case presents an LSB whose leading edge is at $x = 0.38$ and trailing edge at $x = 0.79$ and 0.78 for the rotating and non-rotating cases, respectively. The LSB maximum height $y_{max}/\delta^* = 0.71$ and location $x_{y_{max}} = 0.70$ are the same for both cases. The LSB is divided into two cells of stronger reverse flow, whose generation mechanism may be similar to that discussed for the $AoA = 4.2°$ case. Overall, the LSBs for $\lambda \neq 0$ and $\lambda = 0$ are quite similar, indicating that rotation plays a less important role in cases with low angles of attack.

The results for the pressure side are displayed in Fig. 6. Considering the $AoA = 12.8°$ case, one can notice that the LSBs for rotating and non-rotating simulations do not differ significantly. However, the former presents a longer separation region ($x = 0.47 - 0.92$) compared to the latter ($x = 0.48 - 0.90$), but a slightly lower LSB maximum height ($y_{max}/\delta^* = 0.89$ for the former and $y_{max}/\delta^* = 0.90$ for the latter, both at $x_{y_{max}} = 0.78$). The region with a negative streamwise velocity close to $x = 0$ is generated by the high flow angle that leads the flow to separate between the leading edge and the stagnation point. Regarding the $AoA = 4.2°$ case, there is a large difference between the LSBs in the rotating and non-rotating simulations, particularly in which concerns the reverse flow that is stronger in the former. Moreover, the separation bubble for $\lambda \neq 0$ starts slightly further upstream and reattaches further downstream ($x = 0.36 - 0.97$) than for $\lambda = 0$ ($x = 0.37 - 0.94$). Both cases present $y_{max}/\delta^* = 0.87$, but this value is reached more downstream for the rotating case ($x = 0.79$) compared to the non-rotating one ($x = 0.75$). The $AoA = 1.2°$ case presents similar separation areas for the rotating and non-rotating simulations, displaying a large reverse flow region. Indeed, both cases have the start of the separation at $x = 0.32$ and the flow does not reattach. Moreover, the maximum height of the separation region is $y_{max}/\delta^* = 0.93$ for $\lambda \neq 0$ and $y_{max}/\delta^* = 0.94$ for $\lambda = 0$ at $x_{y_{max}} = 0.83$.

The transition location is assessed with two methods. The first considers it to be the x position where $-\overline{uv}/U_\infty^2 = 0.001$, and the second one the x location of maximum aspect ratio H, as previously mentioned. Figure 7 presents the Reynolds stress on the $x - y$ plane and aspect ratio along x. Considering the $AoA = 12.8°$ case, one can notice that $-\overline{uv}/U_\infty^2$ reaches the threshold of 0.001 at $x = 0.35$ and $x = 0.33$ for the rotating and non-rotating cases, respectively. Notice that the velocity profiles are inflectional as upstream as the leading edge. Still, no instability, manifesting as the rise in the Reynolds stress, seems to develop upstream of the LSB. Moreover, H has a maximum at $x = 0.39$ and $x = 0.36$ for these two simulations, sequentially. Therefore, both indicators show that transition is delayed by rotation on the suction side for this angle of attack. The $AoA = 4.2°$ case presents a Reynolds stress reaching the transition threshold at $x = 0.35$ and $x = 0.36$ for $\lambda \neq 0$ and $\lambda = 0$, respectively. Inflectional velocity profiles occur downstream of $x = 0.22$ and $x = 0.21$, sequentially, which does not seem to give rise to instability directly. The aspect ratio reaches its peak at $x = 0.50$ for both cases. These results indicate that the inception of transition is slightly earlier for the rotating case. The same conclusion can be obtained from the $AoA = 1.2°$ case, which shows $-\overline{uv}/U_\infty^2 = 0.001$ at $x = 0.40$ and $x = 0.41$ for $\lambda \neq 0$ and $\lambda = 0$, respectively, and a maximum aspect ratio at $x = 0.59$. The growth in $-\overline{uv}/U_\infty^2$ precedes the LSB and may be linked to an inviscid instability allowed by the inflectional velocity profiles downstream of $x = 0.28$. It is interesting to notice that the transition pro-

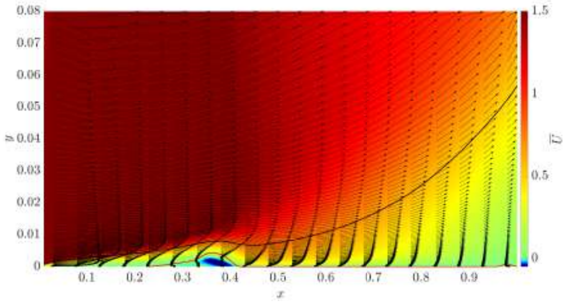

$AoA = 12.8^\circ$ and $\lambda = 0$.

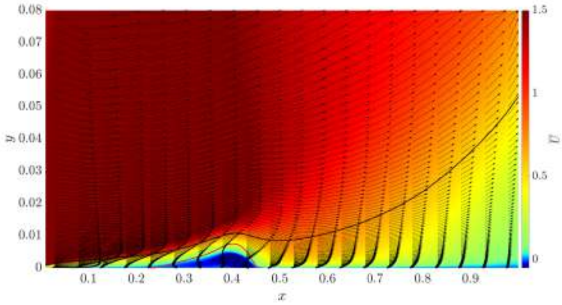

$AoA = 12.8^\circ$ and $\lambda = 4.6$.

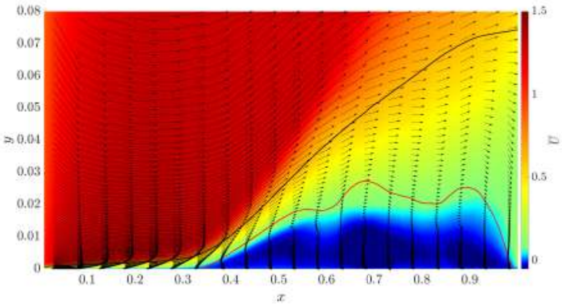

$AoA = 4.2^\circ$ and $\lambda = 0$.

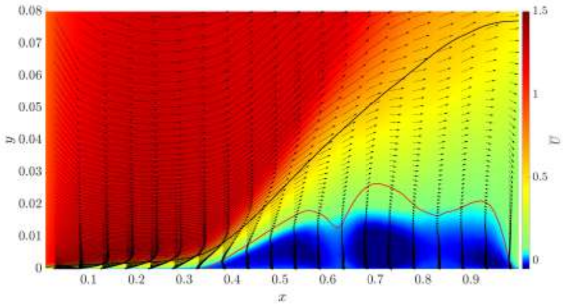

$AoA = 4.2^\circ$ and $\lambda = 9.3$.

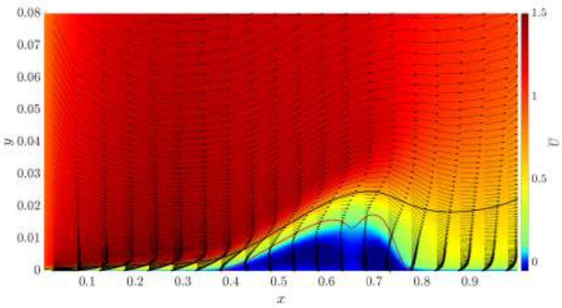

$AoA = 1.2^\circ$ and $\lambda = 0$.

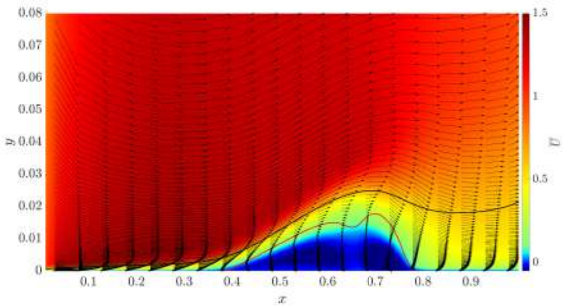

$AoA = 1.2^\circ$ and $\lambda = 13.9$.

Figure 5 – Contours of mean streamwise velocity on the suction side. Red line indicates the boundary of the separation region. Black line highlights the displacement thickness. Vectors represent the the streamwise and normal velocity field.

cess for the $AoA = 12.8^\circ$ case is the fastest one, reaching a maximum in $-\overline{uv}/U_\infty^2$ and H and decaying in a short streamwise extent. Conversely, the slowest transition process is the one for $AoA = 4.2^\circ$, probably due to the massive separation occurring on the suction side, whose flow does not reattach to the airfoil.

The results for the transition location on the pressure side are presented in Fig. 8. Notice that the y scale of the plot for the aspect ratio is in logarithmic scale because the momentum thickness becomes close to zero for the $AoA = 1.2^\circ$ case, making H reaching large values in the separation region. Considering the $AoA = 12.8^\circ$ case, we notice that transition occurs at $x = 0.56$ and $x = 0.61$ for the rotating and non-rotating cases, respectively, according to the Reynolds stress distribution and at $x = 0.70$ and $x = 0.71$, sequentially, from the aspect ratio. However, the velocity profiles become inflectional much upstream, at $x = 0.37$ and $x = 0.38$, for the two mentioned cases, in this order, which does not seem to give rise to instability before the LSB. Thus, the beginning of transition occurs earlier for the rotating case, whereas its achievement occurs at approximately the same location for both cases. The drop in the aspect ratio close to the leading edge for the $AoA = 12.8^\circ$ case is due to the formation of a small LSB caused by an APG. The $AoA = 4.2^\circ$ case presents the onset of transition at $x = 0.37$ and $x = 0.40$ for $\lambda \neq 0$ and $\lambda = 0$, considering the Reynolds stress criterion, and at $x = 0.71$ for both cases considering the maximum aspect ratio. Inflectional velocity profiles occur

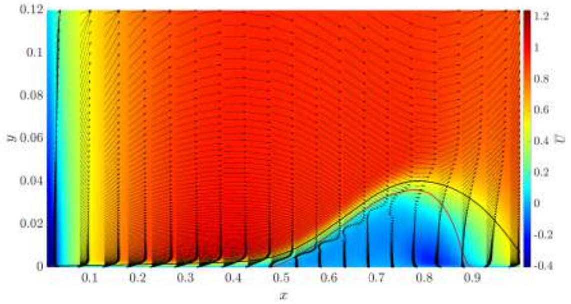

$AoA = 12.8°$ and $\lambda = 0$.

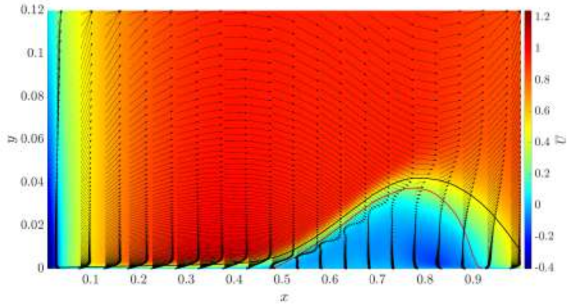

$AoA = 12.8°$ and $\lambda = 4.6$.

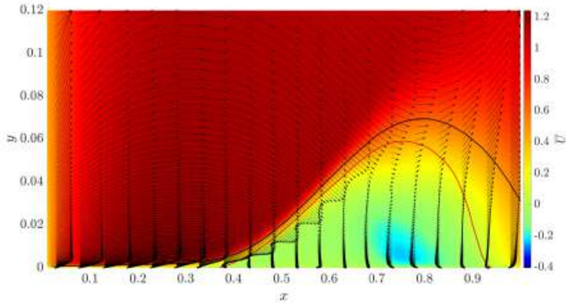

$AoA = 4.2°$ and $\lambda = 0$.

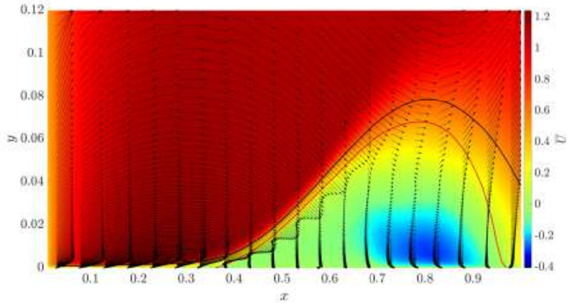

$AoA = 4.2°$ and $\lambda = 9.3$.

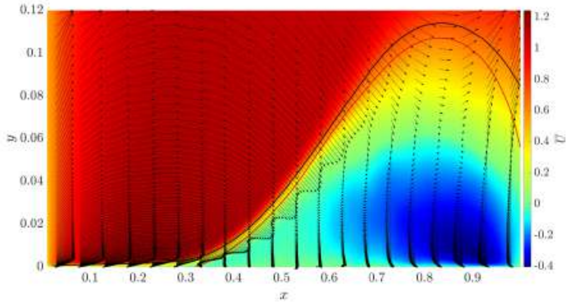

$AoA = 1.2°$ and $\lambda = 0$.

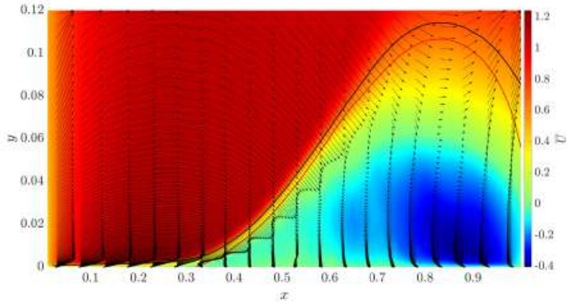

$AoA = 1.2°$ and $\lambda = 13.9$.

Figure 6 – Contours of mean streamwise velocity on the pressure side. Red line indicates the boundary of the separation region. Black line highlights the displacement thickness. Vectors represent the the streamwise and normal velocity field.

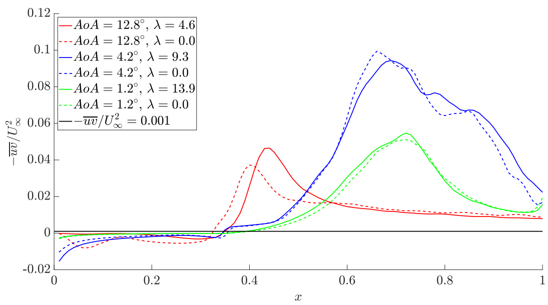

Reynolds stress on the $x-y$ plane along x.

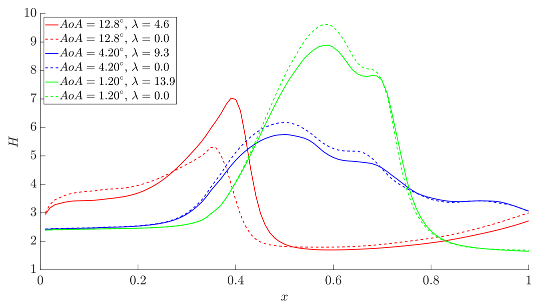

Shape factor as a function of x.

Figure 7 – Analysis of the transition locations on the suction side.

downstream of $x = 0.27$. Finally, the $AoA = 1.2°$ case displays transition at $x = 0.35$ according to the Reynolds stress curves, and at $x = 0.75$ and $x = 0.72$ from the aspect ratio curves for the rotating and non-rotating cases, respectively. However, since H becomes ill-defined for the $AoA = 1.2°$ case, as discussed earlier, the transition location obtained from the aspect ratio may not be accurate. The velocity profiles are inflectional downstream of $x = 0.23$.

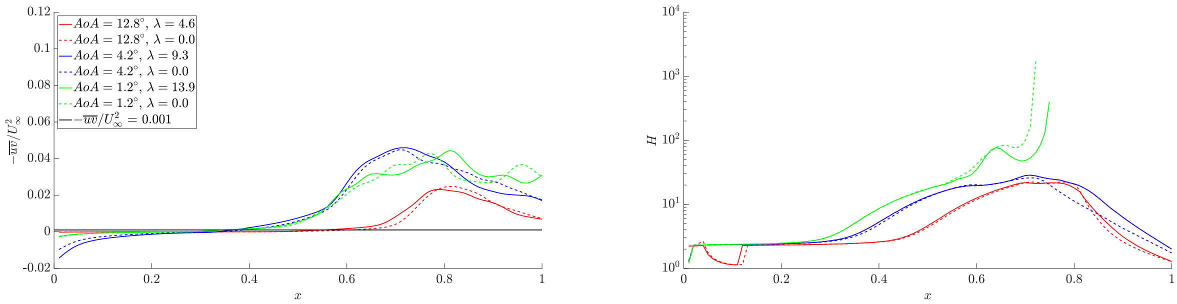

Reynolds stress on the $x-y$ plane along x.

Shape factor as a function of x.

Figure 8 – Analysis of the transition locations on the pressure side.

From the analysis of the transition locations on the pressure and suction sides, it is possible to conclude that rotation has a larger effect on the former, moving the transition location upstream. This is likely because the pressure side presents a milder pressure gradient, with which rotation does not have to compete, and a larger separation region. This is also the case on the suction side for low angles of attack, where the APG is not as strong.

The instantaneous contours of normal velocity fluctuations ($v = V - \langle V \rangle_{z,t}$) over the suction side displayed in Fig. 9 offer an initial explanation for the observed transition behavior. They indicate that, for $AOA = 1.2°$ and $4.2°$, rotation enhances the shear-layer instability, promoting the shedding of higher-amplitude KH rolls, a change that is particularly noticeable in the former case. Moreover, rotation leads to a spanwise modulation of these rolls that is visible in the $AOA = 4.2°$ case, which eventually triggers their break-up to turbulence. The mechanism by which that happens needs further investigation. However, we posit that rotation generates inflectional spanwise velocity profiles that, in turn, lead to unstable spanwise-oscillatory modes [24]. The latter may non-linearly interact with the rolls leading to higher harmonics, and the break-up to turbulence [35, 36]. This would promote a more upstream transition to turbulence than the non-rotating case, where this spanwise modulation is less important. In the $AOA = 12.8°$ case, the phenomenon described above also occurs with the break-up of the KH rolls for $\lambda \neq 0$. However, due to its high AoA, the instabilities generated by rotation cannot surpass the growth of those due to the strong adverse pressure gradient. Instead, the former leads to a partial break-up of the KH rolls with the entrainment of high-momentum fluid into the shear layer and the shear reduction. This causes a reduction in the growth rate of the instabilities due to the APG, and transition is moved downstream.

4. Conclusions

Here, we have studied the effects of rotation on the flow around a thick FFA-W3 series airfoil at a Reynolds number of 100,000 by means of direct numerical simulations. Three angles of attack/rotation speeds were analyzed, where the rotation effects were included as volume forces in the momentum equations (Coriolis and centrifugal forces). Three control simulations with the same angle of attack as the former ones were also performed, for which the volume forces were not included. The mean and instantaneous velocity fields were analyzed to identify the flow features as the separation region and the structures leading to transition. Moreover, the transition locations, lift, and drag coefficients were calculated. The incoming free-stream was laminar but a small amount of noise was introduced inside the boundary-layer to generate some flow perturbations. Its amplitude was kept at very low values such that it did not lead to a 'bypass' transition.

It was found that rotation moves the transition location upstream on the pressure side, and, for relatively low angles of attack, also on the suction side. This possibly occurs due to the enhancement of the shear-layer instability and the spanwise modulation of the Kelvin-Helmholtz (KH) rolls by the inflectional instability of the spanwise velocity profiles generated by rotation. This effect is more pronounced on the pressure side because it presents a milder adverse pressure gradient and larger flow separation. However, rotation moves the transition location downstream on the suction side for larger

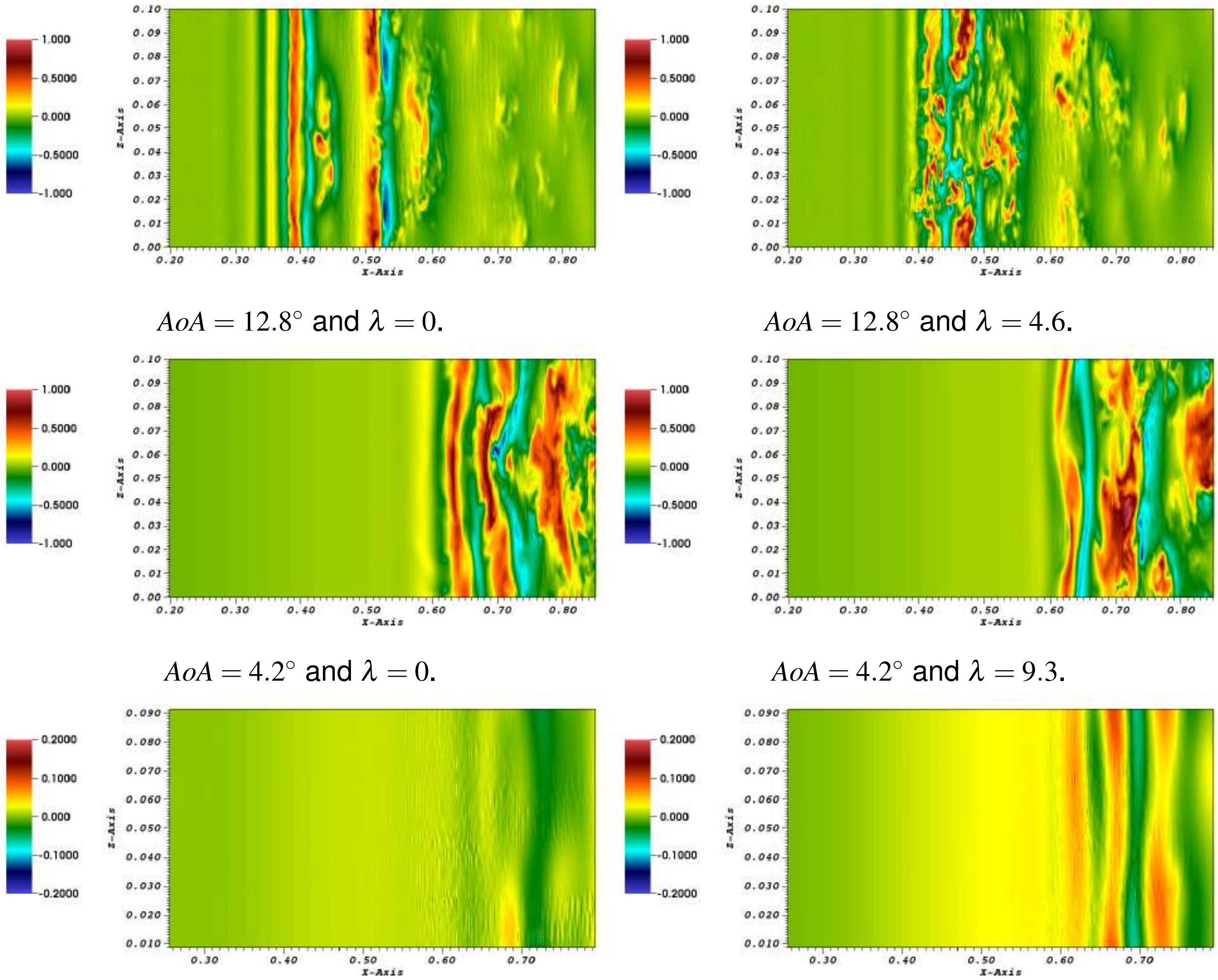

$AoA = 12.8°$ and $\lambda = 0$. $AoA = 12.8°$ and $\lambda = 4.6$.

$AoA = 4.2°$ and $\lambda = 0$. $AoA = 4.2°$ and $\lambda = 9.3$.

$AoA = 1.2°$ and $\lambda = 0$. $AoA = 1.2°$ and $\lambda = 13.9$.

Figure 9 – Instantaneous contours, at an arbitrary time, of normal velocity fluctuations ($v = V - \langle V \rangle_{z,t}$) on a streamwise-spanwise plane over the suction side.

angles of attack (AoA). We posit that, under high AoA, the instabilities generated by rotation cannot surpass those generated by the strong adverse pressure gradient. However, the former can reduce the growth rate of the latter by entraining high-momentum fluid into the shear layer and reducing the shear.

The start of the separation region is almost unaffected by rotation. However, its trailing edge is moved downstream, even when rotation promotes an earlier transition, because the reverse flow is enhanced. Furthermore, the lift was only substantially affected by rotation when there was strong separation on both sides of the airfoil. In this scenario, the lift was degraded due to an increase in the pressure on the suction surface and its decrease on the pressure side.

5. Acknowledgements

This research was supported by StandUp for Energy and carried out within StandUp for Wind. The computations were performed on resources provided by the Swedish National Infrastructure for Computing (SNIC) at the PDC Center for High-Performance Computing at the Royal Institute of Technology (KTH), the National Supercomputer Centre at Linköping University, and the High-Performance Computing Center North (HPC2N) at Umeå University.

6. Copyright Statement

in this paper, to publish it as part of their paper. The authors confirm that they give permission for the publication and distribution of this paper as part of the ICAS proceedings or as individual off-prints from the proceedings.

References

[1] H. Himmelskamp, "Profile investigations on a rotating airscrew," *Reports and Translations*, Völkenrode MAP, Göttingen, Germany, 1947.

[2] W. M. H. Banks and G. E. Gadd, "Delaying effect of rotation on laminar separation," *AIAA Journal*, vol. 1, pp. 941–942, 1963.

[3] W. J. McCroskey and P. F. Yaggy, "Laminar boundary layers on helicopter rotors in forward flight," *AIAA Journal*, vol. 6, pp. 1919–1926, 1968.

[4] J. M. Savino and T. N. Nyland, "Wind turbine flow visualization studies," in *Proceedings of the AWEA Wind Energy Conference, San Francisco, CA*, 1985.

[5] S. J. Schreck, N. N. Sørensen, and M. C. Robinson, "Aeroydnamic structures and processes in rotationally augmented flow fields," *Wind Energy*, vol. 10, pp. 159–178, 2007.

[6] H. Dumitrescu and V. Cardos, "Inboard stall delay due to rotation," *Journal of Aircraft*, vol. 49, pp. 101–107, 2012.

[7] W. J. McCroskey, "Measurements of boundary layer transition, separation and streamline direction on rotating blades," *NASA TN D-6321*, pp. 1–41, 1971.

[8] J. Yang, B. Ganesh, and N. Komerath, "Radial flow measurements downstream of forced dynamic separation on a rotor blade," in *AIAA-Paper, AIAA-2006-3377*, 2006.

[9] J. DiOttavio, K. Watson, J. Cormey, N. komerath, and S. Kondor, "Discrete structures in the radial flow over a rotor blade in dynamic stall," in *AIAA-Paper, AIAA-2008-7344*, 2008.

[10] V. Raghav, P. Richards, N. Komerath, and N. J. Smith, "An exploration of the physics of dynamic stall," in *AHS Aeromechanics Specialists' Conference, San Francisco, CA*, 2010.

[11] Z. Du and M. S. Selig, "The effect of rotation on the boundary layer of a wind turbine blade," *Renewable Energy*, vol. 20, pp. 167–181, 2000.

[12] C. Sicot, P. Devinant, S. Loyer, and J. Hureau, "Rotational and turbulence effects on a wind turbine blade. Investigation of the stall mechanisms," *Journal of Wind Engineering and Industrial Aerodynamics*, vol. 96, pp. 1320–1331, 2008.

[13] L. E. Fogarty, "The laminar boundary layer on a rotating blade," *Journal of Aeronautical Sciences*, vol. 18, pp. 247–252, 1951.

[14] W. Z. Shen and J. N. Sørensen, "Quasi-3D Navier-Stokes model for a rotating airfoil," *Journal of Computational Physics*, vol. 150, pp. 518–548, 1999.

[15] P. K. Chaviaropoulos and M. O. L. Hansen, "Investigating three-dimensional and rotational effects on wind turbine blades by means of a quasi-3D Navier–Stokes solver," *Journal of Fluids Engineering*, vol. 122, pp. 330–336, 2000.

[16] J. C. Narramore and R. Vermeland, "Navier–Stokes calculations on inboard stall delay due to rotation," *Journal of Aircraft*, vol. 29, pp. 73–78, 1992.

[17] D. Hu, O. Hua, and Z. Du, "A study on stall-delay for horizontal axis wind turbine," *Renewable Energy*, vol. 31, pp. 821–836, 2006.

[18] M. A. Potsdam and D. J. Mavriplis, "Unstructured mesh CFD aerodynamic analysis of the NREL Phase VI rotor," in *AIAA-Paper, AIAA-2009-1221*, 2009.

[19] G. Bangga, T. Lutz, E. Jost, and E. Krämer, "CFD studies on rotational augmentation at the inboard sections of a 10 MW wind turbine rotor," *Journal of Renewable and Sustainable Energy*, vol. 9, pp. 1–24, 2017.

[20] S. G. Horcas, F. Debrabandere, B. Tartinville, C. Hirsch, and G. Coussement, "Rotor-tower interactions of DTU 10MW reference wind turbine with a non-linear harmonic method," *Wind Energy*, vol. 20, pp. 619–636, 2016.

[21] J. Johansen, N. N. Sørensen, J. A. Michelsen, and S. Schreck, "Detached-eddy simulation of flow around the NREL Phase VI blade," *Wind Energy*, vol. 5, pp. 185–197, 2002.

[22] S. A. E. Miller and P. J. Miller, "Rotational effects on the aerodynamics of wind turbine airfoils," in *AIAA-Paper, AIAA-2006-2575*, 2006.

[23] C. Stone, C. E. Lynch, and M. J. Smith, "Hybrid RANS/LES simulations of a horizontal axis wind turbine," in *AIAA-Paper, AIAA-2010-459*, 2010.

[24] A. Gross, H. F. Fasel, T. Friederich, and M. J. Kloker, "Numerical investigation of rotational augmentation for S822 wind turbine airfoil," *Wind Energy*, vol. 15, pp. 983–1007, 2012.

[25] Z. Jing, A. Ducoin, and C. Braud, "Direct numerical simulation of transitional boundary layers on a horizontal axis wind turbine blade," *Journal of Physics: Conference Series*, vol. 1618, pp. 1–10, 2020.

[26] Z. Jing and A. Ducoin, "Direct numerical simulation and stability analysis of the transitional boundary layer on a marine propeller blade," *Physics of Fluids*, vol. 32, pp. 1–15, 2020.

[27] H. L. Reed and W. S. Saric, "Stability of Three Dimensional Boundary Layers," *Annual Review of Fluid Mechanics*, vol. 21, pp. 235–284, 1989.

[28] T. C. L. Fava, M. Lokatt, N. Sørensen, F. Zahle, A. Hanifi, and D. Henningson, "A simplified model for transition prediction applicable to wind-turbine rotors," *Wind Energy Science*, vol. 6, pp. 715–736, 2021.

[29] A. Björck, "Coordinates and calculations for the FFA-W1-xxx, FFA-W2-xxx and FFA-W3-xxx series of airfoils for horizontal axis wind turbines," *FFA TN 1990-15*, pp. 1–148, 1990.

[30] C. Bak, R. D. Bitsche, A. Yde, and T. Kim, "Light Rotor: The 10-MW reference wind turbine," in *Proceedings of EWEA 2012 - European Wind Energy Conference & Exhibition*, 2012.

[31] P. F. Fischer, J. W. Lottes, and S. G. Kerkemeier, "*Nek5000 web page*," 2008. http://nek5000.mcs.anl.gov.

[32] ANSYS, Inc., "*ANSYS Fluent User's Guide*," 2015. Canonsburg, PA, USA, Release 16.1.

[33] W. Yuan, M. Khalid, J. Windte, U. Scholz, and R. Radespiel, "An investigation of low–Reynolds number flows past airfoils," in *Proceedings of 23rd AIAA Applied Aerodynamics Conference, Toronto, Ontario, Canada, June 6–9*, 2005.

[34] S. Burgmann and W. Schröder, "Investigation of the vortex induced unsteadiness of a separation bubble via time-resolved and scanning PIV measurements," *Experiments in Fluids*, vol. 45, pp. 675–691, 2008.

[35] O. Marxen, M. Lang, U. Rist, and S. Wagner, "A combined experimental/numerical study of unsteady phenomena in a laminar separation bubble," *Flow, Turbulence and Combustion*, vol. 71, pp. 133–146, 2003.

[36] O. Marxen and U. Rist, "Mean flow deformation in a laminar separation bubble: separation and stability characteristics," *Journal of Fluid Mechanics*, vol. 660, pp. 37–54, 2010.